Neutron Generation by Laser-Driven Spherically Convergent Plasma Fusion

G. Ren,[1] J. Yan,[2] J. Liu,[1,3,4,*] K. Lan,[1] Y. H. Chen,[1] W. Y. Huo,[1] Z. Fan,[1] X. Zhang,[2] J. Zheng,[2] Z. Chen,[2] W. Jiang,[2] L. Chen,[2] Q. Tang,[2] Z. Yuan,[2] F. Wang,[2] S. Jiang,[2] Y. Ding,[2] W. Zhang,[1,3] and X. T. He[1,3]

[1]*Institute of Applied Physics and Computational Mathematics, Beijing 100088, China*

[2]*Research Center of Laser Fusion, Chinese Academy of Engineering Physics, Mianyang 621900, China*

[3]*Center for Applied Physics and Technology, Peking University, Beijing 100871, China*

[4]*Collaborative Innovation Center of IFSA, Shanghai Jiao Tong University, Shanghai 200240, China*

(Received 14 December 2016; published 19 April 2017)

We investigate a new laser-driven spherically convergent plasma fusion scheme (SCPF) that can produce thermonuclear neutrons stably and efficiently. In the SCPF scheme, laser beams of nanosecond pulse duration and 10^{14}–10^{15} W/cm^2 intensity uniformly irradiate the fuel layer lined inside a spherical hohlraum. The fuel layer is ablated and heated to expand inwards. Eventually, the hot fuel plasmas converge, collide, merge, and stagnate at the central region, converting most of their kinetic energy to internal energy, forming a thermonuclear fusion fireball. With the assumptions of steady ablation and adiabatic expansion, we theoretically predict the neutron yield Y_n to be related to the laser energy E_L, the hohlraum radius R_h, and the pulse duration τ through a scaling law of $Y_n \propto (E_L/R_h^{1.2}\tau^{0.2})^{2.5}$. We have done experiments at the ShengGuangIII-prototype facility to demonstrate the principle of the SCPF scheme. Some important implications are discussed.

DOI: 10.1103/PhysRevLett.118.165001

Introduction.—Neutron sources have important applications in many fields of science and engineering including the nuclear fuel cycle, neutron activation analysis, mineral and petroleum exploration, etc. Among the many ways to produce neutrons, which are usually based on high-energy accelerators and fission reactors through isotope disintegration and spallation, the laser-driven neutron sources are of particular interest and have attracted much attention recently [1–4].

The laser cluster interactions (LCIs) use an intense (10^{16}–10^{18} W/cm^2) femtosecond laser to strip off peripheral electrons from deuterium-tritium (DT) clusters of 10^3–10^5 atoms, forming DT ion clusters with positive charges, triggering a Coulomb explosion which accelerates the DT ions to an energy of several million electron volts (MeV). The collisions between the high-energy ions result in nuclear fusion reactions. The LCI approach can be implemented in a tabletop size, but the neutron yield is low, around 10^7 per laser pulse [1,2]. With a laser of picosecond pulse and higher intensity (10^{20}–10^{21} W/cm^2), the laser target interaction approach (LTI) [3] can accelerate deuterons to 100 MeV energies that are dumped in low-Z converter (Be) targets to produce neutrons via the nuclear reaction $^9\mathrm{Be}(d,n)$. This approach has produced a high neutron flux of 10^{10}/sr. However, the neutron spectrum is distributed widely from a few MeV to 100 MeV.

On the other hand, for the laser-driven implosions of a DT capsule by direct drive [5–7] and indirect drive [4], the neutron yield can reach as high as 5×10^{13} on the 30 kJ Omega laser [8] and 9×10^{15} on the 1.8 MJ National Ignition Facility (NIF) laser [9,10], respectively. Nevertheless, these inertial implosion schemes require a high convergence ratio (~30), and the implosions are often degraded by hydrodynamic instabilities [11–14] and laser plasma instabilities [15] as well as radiation asymmetry [16]. Other interesting approaches include the laser-driven exploding pusher target [17], shock ignition [18] and laser-assisted magnetized liner inertial fusion [19,20], etc.

In this Letter, we investigate a new laser-driven scheme of spherically convergent plasma fusion (SCPF) that can generate a thermonuclear fusion neutron efficiently and robustly. Theoretically, we have modeled the ion temperature and density of converging hot plasmas and derived an explicit scaling law of the neutron yield with respect to laser parameters and target radius. In particular, we have performed experiments to demonstrate the principle of SCPF at the ShengGuangIII-prototype (SGIII-proto) facility. In the experiment, we have obtained a maximum deuterium-deuterium (DD) fusion neutron yield of 3.5×10^9 with a 6.3 kJ laser. The ion temperature is about 7 keV. The observed dependence of the neutron yields on the laser and target parameters agrees with our theoretical prediction. We further discuss the optimization of the SCPF scheme and some important implications.

SCPF principle and scaling law.—In the SCPF scheme, we suppose multiple laser beams of nanosecond (ns) duration and 10^{14}–10^{15} W/cm^2 intensities uniformly irradiate and ablate the thermonuclear fuel layer (~20 μm) lined inside a spherical hohlraum [Fig. 1(a)]. The fuel layer expands and implodes towards the center [Fig. 1(b)], and eventually the hot fuel plasmas converge and stagnate at the central region of the sphere [Fig. 1(c)], converting most of

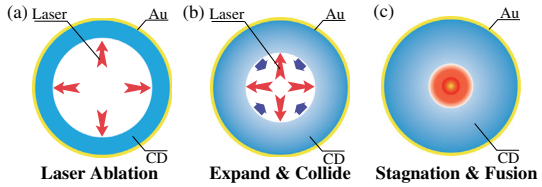

FIG. 1. Schematic plot of laser-driven spherically convergent plasma fusion processes.

their kinetic energy to the internal energy, raising the ion temperature to around 10 keV, and causing thermonuclear fusion reactions to occur.

For the nanosecond laser ablation of the low-Z fuel layer, such as deuterated polystyrene (CD), a laser-driven stationary ablation model for a spherical target can be properly exploited [21]. The mass ablation rate $\dot{m}$ and ablating plasma temperature T_{ab} can be deduced as $\dot{m} \propto I_L^{0.76}$ and $T_{ab} \propto I_L^{2/3}$, respectively, where I_L denotes the laser intensity. Meanwhile, the plasmas expand at a velocity of v_i related to the acoustic speed of the ablated hot plasmas, $v_i \propto T_{ab}^{1/2} \propto I_L^{1/3}$.

The ablating plasmas expand, collide, and stagnate at the sphere center. At stagnation, the kinetic energy is converted into ion thermal energy, making the ion temperature T_i increase dramatically, i.e., $T_i \propto v_i^2 \propto I_L^{2/3}$; here, we assume approximately that for the ablated plasmas the ions expand adiabatically [22].

The total neutron yield equals the nuclear reaction rate integrated over the plasma volume and confinement time, i.e., $Y_n = \frac{1}{2} n_D^2 \langle \sigma v \rangle_{\mathrm{DD}} V \Delta t$, where the plasma number density $n_D = N/V$ with $N \sim \dot{m} S_{\mathrm{spot}} \tau$, where S_{spot} is the total area of the laser spots that is proportional to πR_h^2, R_h is the radius of the sphere hohlraum, and τ is the laser pulse length. The average reactivity of deuterium on deuterium is proportional to T_i^2 near 10 keV. V is the burn plasma volume of radius $R_c \propto R_h$ according to the pressure balance principle, and Δt is the fusion burn time, which is proportional to R_c / v_{shock} with $v_{\mathrm{shock}} \propto \sqrt{T_i}$ the speed of the outward propagating shock after stagnation. We finally obtain [22]

$$Y_n \propto \left(\frac{E_L}{R_h^{1.2} \tau^{0.2}} \right)^{2.5} = D^{2.5}, \tag{1}$$

where $D = E_L / R_h^{1.2} \tau^{0.2}$ served as the scaling parameter for the SCPF and E_L is the laser energy which is related to the intensity through $E_L = I_L \tau S_{\mathrm{spot}}$.

The above deductions indicate that the SCPF neutron yield is proportional to the incident laser energy to the power of 2.5. For the laser-driven capsule implosion, the scaling is $Y_n \propto {E_L}^3$ without alpha-particle self-heating; it rises to $Y_n \propto {E_L}^{4\text{–}5.8}$ with alpha-particle self-heating [27] and is expected to rise further with the realization of ignition and burn. In contrast, for the LTI scheme the yield scaling is roughly $Y_n \propto E_L$ [3], and for the LCI scheme the yield scaling is roughly $Y_n \propto {E_L}^2$ [2].

A few other related fusion concepts based on the spherical configuration have been discussed previously. The spherically convergent ion focus [28] uses electrostatic confinement where ions are accelerated towards a spherical cathode. The fusion occurs mainly by beam-beam or beam-target interactions, and therefore the fusion reactions are not fully thermonuclear and, consequently, may be limited to low gains.

The plasma-jet-driven magneto-inertial fusion (PJMIF) uses a spherical array of plasma guns to generate plasma jets which merge and form an imploding plasma liner to compress preheated magnetized target plasmas to thermonuclear condition [29,30]. Both PJMIF and our SCPF make use of the center-oriented plasma motion and spherical convergence to amplify the imploding power density of the converging plasmas by several orders of magnitude. However, in our SCPF scheme, because the lasers are capable of delivering a power density orders of magnitude higher than the plasma guns, the initial power density of the ablated plasmas in the SCPF can be orders of magnitude higher than the plasma jets produced in PJMIF.

Experiment setup.—To demonstrate the SCPF principle, we have performed experiments at the SGIII-proto laser facility. The SGIII-proto laser is a neodymium glass laser operating at triple frequency with the wavelength of 351 nm. It has eight laser beams with four beams on each end, outputting 8 kJ energy at maximum and a pulse duration from 1 to 3 ns. We fabricate spherical hohlraums out of gold with a shell thickness of 25 μm and two laser entrance holes (LEHs) at the poles. The gold spherical hohlraum has an inner diameter of 1700 μm. The diameter of the LEHs is 1000 μm. We line the wall of the gold hohlraum with CD of 40 μm in depth. We also fabricate some smaller hohlraums with an inner diameter of 1500 μm.

The experimental setup is shown in Fig. 2. The laser beams are aligned in two conical rings and enter the hohlraum through the LEHs. The beam angle with respect to the vertical hohlraum axis is 45°. Usually, the diameter of the laser spots is 500 μm with the smoothing technique of the continuous phase plate (CPP). We also conduct experiments in which the laser spot size is 200 μm without using the CPP. We use one scintillator (Sc.D1 in Fig. 2) to count the neutron yield, another one (Sc.D2 in Fig. 2) to measure the neutron bang time, and a neutron time of flight (nTOF) measurement to infer the DD ion temperature. We use a gated x-ray image (GXI) camera to capture time-resolved x-ray pictures of the plasma converging process. The x-ray flux flowing out of the LEH is measured using an absolutely calibrated flat-response x-ray diode (FXRD). Laser injection is monitored by using a pinhole x-ray camera (PHC). Laser backscatterings are measured by a full

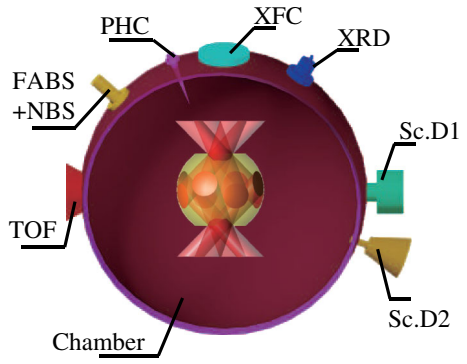

FIG. 2. Illustration of the experimental setup, and the to-scale side-on view of the two-LEH spherical hohlraum with laser beams.

aperture backscattering system (FABS) and a near backscattering system (NBS) and to be less than 10% in our experiments. Note that for the low-Z CD hohlraum the radiation temperature is as low as 130 eV, which cannot affect the plasma dynamics significantly.

Experimental results and discussion.—The GXI camera measuring x-ray emission above 2 keV is positioned to image emissions through the LEH to investigate the plasma converging processes. Clear and time-resolved pictures are successfully caught as shown in Fig. 3(a). In each image in Fig. 3(a), the outer ring is the image of the x-ray emission from the edge of the LEH. We will address the central portion of the image that is caused by the emissions emanating from the converging plasmas. Clear bright emissions are observed from 0.8 to 1.0 ns. We believe these are emitted by colliding high-speed plasma jets squeezed out by adjacent laser ablated bubbles [31], which soon fade away because of the rapid electron energy loss due to the bremsstrahlung emission and plasma rarefaction. Since the x-ray emissions appear at 0.8 ns, we estimate the

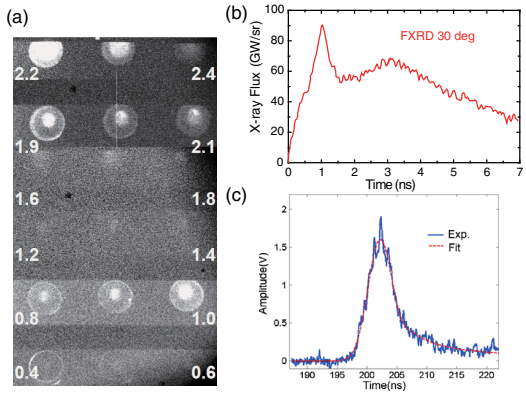

FIG. 3. In the panel, (a) is the GXI images of the convergent plasma emission above 2 keV with the time pinpointed, and the gate time is 70 ps; (b) is the temporal x-ray flux measured by FXRD with an energetic range from 100 eV to 4.4 keV from LEH with 30° to the axis; (c) is the nTOF line with a fitting curve.

velocity of the plasma jets to be about 1000 km/s, which is about 4 times the sound speed [32,33]. From 1.0 to 1.8 ns, the images become dark at the center. Note that the neutron peak emission time or the bang time is in between, i.e., about 1.5 ns. From 1.9 to 2.4 ns, brighter and larger emissions are seen again. We believe the second round of bright emissions are the x rays emitted by the converged wall plasmas ablated by the lasers.

In Fig. 3(b), we observe the spectrally integrated x-ray flux measured by FXRD through the LEH at an angle of 30° to the axis. From this direction, the FXRD views emissions from both the hohlraum wall area and the central region. The x-ray flux rises quickly during the first 1 ns when the laser beams are on, and it is contributed mostly by the emissions from the ablation of the hohlraum wall by the lasers. After the lasers are turned off at 1.0 ns, the x-ray flux drops quickly. At around 2.0 ns, the flux begins to rise slowly again and reaches a second peak at 3.3 ns. After 3.3 ns, the x-ray flux drops slowly and lasts for several nanoseconds. The second flux hump is associated with the emission of converging plasmas; it stands for a longer time and fades away slower.

In Fig. 3(c), the nTOF signal is fitted reasonably well by assuming a thermonuclear DD reaction of plasma with an ion temperature of 6.6 keV, confirming our theory of convergent plasma thermalization and concomitant thermonuclear fusion rather than other fusion mechanisms. The above thermalized plasma fusion picture is consistent with our estimated ion equilibration time of the order of a few picoseconds [22].

The neutron bang time of 1.5 ns is about 0.4 ns earlier than the second round of hard x-ray emission in GXI and 1.8 ns earlier than the FXRD second emission peak, reflecting intrinsically the electron-ion relaxation and nonequilibrium energy transfer in the processes of plasma convergence and subsequent outward shock propagation [22]. The bubble implosion speed is estimated to be around 500 km/s calculated by the inner radius of the hohlraum (810 μm) divided by 1.5 ns transit time. When the plasmas converge into the sphere center at about 1.5 ns, the ion temperature reaches its peak value of about 7 keV due to kinetic-thermal energy conversion. At this time, the plasmas have an apparent accumulation at the central region yielding a maximum neutron generation.

The 0.4 ns time delay of the hard x-ray emission to the neutron bang time is due to the fact that the ions are soon thermalized in a few picoseconds while the electron temperature rise is through an ion-electron relaxation of ~0.7 ns time scale, with considering typical SCPF plasma parameters of $T_e = 2$ keV, $T_i = 7$ keV, and $n_i = 1.5 \times 10^{21}/\mathrm{cm}^3$ according to our simulations [22]. The electron temperature remains low until 1.9 ns, leading to the dark image recorded by GXI. From 1.9 to 2.3 ns, the electron temperature rises to a certain level above 2 keV due to ion-electron energy relaxation, and the GXI images

can be seen clearly. After 2.3 ns, the electron energy loss through bremsstrahlung emission leads to the fadeaway of GXI images, while the FXRD signals can still increase until 3.3 ns. This is because the FXRD of broadly spectrum-integrated x-ray flux are not so sensitive to the electron temperature, and the FXRD view field is large and can receive emissions from both the central and the peripheral plasmas. The peripheral low-density plasmas are compressed and heated to consecutively emit x rays when swept by the outgoing shock [22]. The shock effect and the time delay between neutron and x-ray emissions also emerged in capsule implosion experiments [24].

Our radiation hydrodynamic simulations with the LARED code [25] corroborate the above thermalization and relaxation pictures [22]. The nonequilibrium plasmas with a higher ion temperature and a lower electron temperature are desirable for nuclear fusion, because it increases the fusion reactivity and at the same time reduces energy losses through electron bremsstrahlung emission [34].

The neutron yields are measured by a plastic scintillator. The highest neutron yield is 3.5×10^9 achieved using a smaller hohlraum with a diameter of 1500 μm and an input laser energy of 6.3 kJ. It is worth mentioning that the neutron yields are remarkably stable. Three consecutive shots are fired with the 1700 μm hohlraum and a laser energy of 6.1, 5.9, and 5.8 kJ. The corresponding neutron yields are 3.2×10^9, 2.8×10^9, and 2.9×10^9, respectively. With all the experimental variations, such as the laser shot-to-shot energy variation and the target fabrication imperfections, the robustness in neutron yields is clearly evident. According to the nTOF measurement, the ion temperatures are typically around 6–8 keV, which are apparently higher than the 3–5 keV seen in NIF inertial implosions [35].

A total of 11 laser shots are fired, and neutron yield data are collected. In Fig. 4, the red stars show the neutron yield produced by a hohlraum with a diameter of 1700 μm and a laser spot diameter of 500 μm. The number of laser beams is adjusted to give the required total laser energies. The red

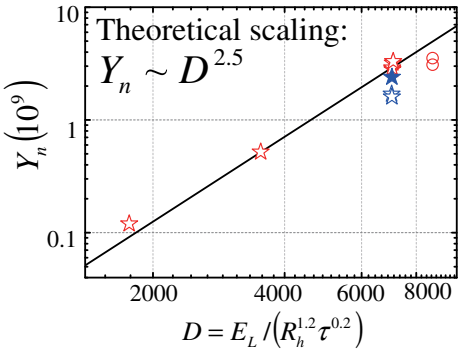

FIG. 4. The neutron yield data versus the scaling parameter. The error bars of the data are about 10%–15%, approximately equivalent to the vertical size of the varied scatters. E_L in units of J, R_h in units of mm, and τ in units of ns. Different scatters represent varied parameters; refer to the text for details.

circles represent the data with a smaller hohlraum of 1500 μm diameter. The hollow blue stars in Fig. 4 are yields obtained with a hohlraum of 1700 μm diameter and smaller laser spots of 200 μm diameter. Figure 4 shows that the neutron yield data are in agreement with the theoretical scaling law.

Two laser spot sizes with diameters of 500 and 200 μm are used to study the neutron yield dependency on spot sizes. As shown in Fig. 4, with the other target and laser parameters remaining identical, the yields with big spots (red stars) are about 50% higher than those with small spots (blue hollow stars). Though the plasma temperature with big spots is lower than that with small spots, the ablated mass is larger, giving rise to a larger fuel density at convergence and a longer confinement time.

We intentionally move the laser pointing location to form two distinct geometrical configurations to investigate yield dependency on geometric symmetry. The first configuration consists of one ring of laser spots on the equator. The second configuration has two rings of spots on each side of the equator with a distance of 600 μm between two rings. The first configuration gives the neutron yield of 1.7×10^9 and ion temperature of 6.4 keV (blue hollow stars in Fig. 4), while the second configuration gives 2.4×10^9 with an ion temperature of 7.6 keV (blue solid star in Fig. 4). Our interpretation is that, with one equatorial ring of laser spots, the colliding plasmas will eventually form a more cylindrical shape of hot dense plasmas (2D convergence), while in the second situation the colliding plasmas will form a relatively more spherical shape of hot dense plasma (3D convergence). In the latter case, the higher-dimensional convergence leads to a higher stagnation density and a higher ion temperature. For this reason, the octahedral spherical hohlraum [36,37] with six LEHs is a better choice for the SCPF scheme, because with the six-LEH the convergent plasmas are more spherically symmetric than that with two-LEH used in our experiment.

The choice of fuel material for the ablation layer is crucial for the SCPF. The neutron yield of different materials depends not only on their reactivity but also on the average atomic number A and average nuclear charge number Z through $Y_n \propto (A/Z)^{1/3}(1+Z)^{-1.5}A^{-0.5}$ [22]. For cryogenic DT, we expect to achieve a higher neutron yield of $Y_{\mathrm{DT}} = 12 r_{\sigma v} Y_{\mathrm{CD}}$ with $r_{\sigma v} = \langle \sigma v \rangle_{\mathrm{DT}}/\langle \sigma v \rangle_{\mathrm{DD}}$ the ratio of DT fusion reactivity to DD fusion reactivity. It indicates that the 3.5×10^9 DD neutron yield obtained in the current experiment is equivalent to the 4.2×10^{12} DT neutron. Moreover, according to the scaling law of the SCPF, one might expect to achieve $\sim 3.0 \times 10^{13}$ DT neutrons on the 30 kJ Omega laser with the spherical hohlraum diameter of 3.4 mm and a duration of 1 ns and $\sim 3.2 \times 10^{17}$ DT neutrons on the 1.8 MJ NIF laser with the spherical hohlraum diameter of 5.6 mm and a duration of 3 ns. The fusion energy can even balance or exceed the input energy with a laser energy larger than 3.3 MJ and a properly designed SCPF target.

In summary, the concept of laser-driven spherical convergent plasma fusion is proposed and investigated, and its principle has been demonstrated experimentally at the SGIII-prototype laser facility. It is shown that the SCPF scheme is efficient, robust, and insensitive to experimental variations, and the neutron yield can be predicted by our simple scaling law. The SCPF concept has important implications in neutron source and proton diagnostics. It can be further optimized by shaping the laser pulse or raise the convergent plasma temperature with fast heating by directly driven lasers [38,39], etc. Related works are ongoing.

This work is supported by the National Basic Research Program of China (2013CB834100), National Natural Science Foundation of China under Grants No. 11475027, No. 11674034, and No. 11475032.

*liu_jie@iapcm.ac.cn

[1] T. Ditmire, J. W. G. Tisch, E. Springate, M. B. Mason, N. Hay, R. A. Smith, J. Marangos, and M. H. R. Hutchinson, Nature (London) **386**, 54 (1997).
[2] T. Ditmire, J. Zweiback, V. P. Yanovsky, T. E. Cowan, G. Hays, and K. B. Wharton, Phys. Plasmas **7**, 1993 (2000).
[3] M. Roth *et al.*, Phys. Rev. Lett. **110**, 044802 (2013).
[4] J. D. Lindl, P. Amendt, R. L. Berger, S. Gail Glendinning, S. H. Glenzer, S. W. Haan, R. L. Kauffman, O. L. Landen, and L. J. Suter, Phys. Plasmas **11**, 339 (2004).
[5] R. L. McCrory *et al.*, Phys. Plasmas **15**, 055503 (2008).
[6] V. N. Goncharov *et al.*, Phys. Rev. Lett. **104**, 165001 (2010).
[7] T. J. B. Collins *et al.*, Phys. Plasmas **19**, 056308 (2012).
[8] S. P. Regan *et al.*, Phys. Rev. Lett. **117**, 025001 (2016).
[9] O. A. Hurricane *et al.*, Nature (London) **506**, 343 (2014).
[10] T. Döppner *et al.*, Phys. Rev. Lett. **115**, 055001 (2015).
[11] L. Rayleigh, Proc. London Math. Soc. **14**, 170 (1883); G. I. Taylor, Proc. R. Soc. A **201**, 192 (1950).
[12] R. D. Richtmyer, Commun. Pure Appl. Math. **13**, 297 (1960); E. E. Meshkov, Fluid Dyn. **4**, 101 (1972).
[13] H. Helmholtz, Philos. Mag. **36**, 337 (1868); W. Thomson, Philos. Mag. **42**, 362 (1871).
[14] T. Ma *et al.*, Phys. Rev. Lett. **111**, 085004 (2013).
[15] R. K. Kirkwood *et al.*, Plasma Phys. Controlled Fusion **55**, 103001 (2013).
[16] R. H. H. Scott *et al.*, Phys. Rev. Lett. **110**, 075001 (2013).
[17] M. J. Rosenberg *et al.*, High Energy Density Phys. **18**, 38 (2016).
[18] R. Betti and O. A. Hurricane, Nat. Phys. **12**, 717 (2016).
[19] S. A. Slutz, M. C. Herrmann, R. A. Vesey, A. B. Sefkow, D. B. Sinars, D. C. Rovang, K. J. Peterson, and M. E. Cuneo, Phys. Plasmas **17**, 056303 (2010).
[20] M. R. Gomez *et al.*, Phys. Rev. Lett. **113**, 155003 (2014).
[21] S. Atzeni and J. Meyer-ter-vehn, *The Physics of Inertial Fusion* (Clarendon, Oxford, 2004).
[22] See Supplemental Material at http://link.aps.org/supplemental/10.1103/PhysRevLett.118.165001 for the detailed deduction of the scaling law, discussion of relaxation rate, the time scales for neutron and x-ray emissions, and some hydrodynamic simulations, which includes Refs. [21,23–26].
[23] J. Wesson, *Tokamaks* (Clarendon, Oxford, 2003).
[24] S. Le Pape *et al.*, Phys. Rev. Lett. **112**, 225002 (2014).
[25] Z. Fan, S. Zhu, W. Pei, W. Ye, M. Li, X. Xu, J. Wu, Z. Dai, and L. Wang, Europhys. Lett. **99**, 65003 (2012).
[26] E. L. Dewald *et al.*, Phys. Rev. Lett. **95**, 215004 (2005).
[27] O. A. Hurricane *et al.*, Nat. Phys. **12**, 800 (2016).
[28] T. A. Thorson, R. D. Durst, R. J. Fonck, and A. C. Sontag, Nucl. Fusion **38**, 495 (1998).
[29] Y. C. F. Thio, J. Phys. Conf. Ser. **112**, 042084 (2008).
[30] Y. C. F. Thio, C. E. Knapp, R. C. Kirkpatrick, R. E. Siemon, and P. J. Turchi, J. Fusion Energy **20**, 1 (2001).
[31] S. H. Glenzer *et al.*, Phys. Plasmas **6**, 2117 (1999).
[32] C. K. Li *et al.*, Phys. Rev. Lett. **102**, 205001 (2009).
[33] C. K. Li *et al.*, Science **327**, 1231 (2010).
[34] Z. Fan, J. Liu, B. Liu, C. Yu, and X. T. He, Phys. Plasmas **23**, 010703 (2016).
[35] A. L. Kritcher *et al.*, Phys. Plasmas **23**, 052709 (2016).
[36] K. Lan, J. Liu, D. Lai, W. Zheng, and X.-Tu He, Phys. Plasmas **21**, 010704 (2014).
[37] K. Lan *et al.*, Matter Radiat. Extremes **1**, 8 (2016).
[38] Y. Kitagawa *et al.*, Phys. Rev. Lett. **108**, 155001 (2012).
[39] Y. Mori *et al.*, Phys. Rev. Lett. **117**, 055001 (2016).